Article

Photothermal Killing of A549 cells and Autophagy Induction by Bismuth Selenide Nanoparticles

Yue You [1,§], Jinxia Li [1,§], Linlin Chen [1], Mei Wang [1], Xinghua Dong [1], Liang Yan [1], Aiping Zhang [2], Feng Zhao [1,*]

[1] CAS Key Laboratory for Biomedical Effects of Nanomaterials and Nanosafety, Institute of High Energy Physics, Chinese Academy of Sciences (CAS), Beijing 100049, China; youyue@ihep.ac.cn; lijinxia@ihep.ac.cn; chenll@ihep.ac.cn; wangmei@ihep.ac.cn; dongxh@ihep.ac.cn; yanliang@ihep.ac.cn;
[2] College of Pharmacy, Shanxi Medical University, Taiyuan 030001, China; zhangap1@163.com
* Correspondence: zhaof@ihep.ac.cn
§ These authors contributed equally

Abstract: With a highly efficient optical absorption capability, bismuth selenide (Bi_2Se_3) nanomaterial can be used as an outstanding photothermal agent for anti-tumor treatment and shows promise in the field of nanotechnology-based biomedicine. However, little research has been done on the relevant mechanism underlying the photothermal killing effect of Bi_2Se_3 nanomaterial. Herein, the photothermal effects of Bi_2Se_3 nanoparticles on A549 cells were explored with emphasis put on autophagy. Firstly, we characterized the structure and physicochemical property of the synthesized Bi_2Se_3 and confirmed their excellent photothermal conversion efficiency (35.72%), photostability, biocompatibility and ability of photothermal killing on A549 cells. Enhanced autophagy was detected in Bi_2Se_3-exposed cells under an 808 nm laser. Consistently, an elevated expression ratio of LC3-II to LC3-I, a marker of autophagy occurrence, was induced in Bi_2Se_3-exposed cells upon NIR irradiation. Meanwhile, the expression of cleaved-PARP was increased in the irradiated cells dependently on the exposure concentrations of Bi_2Se_3 nanoparticles. Pharmacological inhibition of autophagy by 3-methyladenine (3-MA) further strengthened the photothermal killing effect of Bi_2Se_3. Meanwhile, stress-related signaling pathways including p38 and SAPK/JNK were activated coupled with the attenuated PI3K/Akt signaling. Our study figures out that autophagy and the activation of stress-related signaling pathways were involved in the photothermal killing of cancerous cells by Bi_2Se_3, which provides a more understanding of photothermal nanomaterials.

Keywords: bismuth selenide nanoparticles, photothermal killing, apoptosis, autophagy, stress-related signaling pathway

1. Introduction

Nowadays, cancer remains a great threat to human health worldwide. The development of strategies to completely cure cancer is still a great challenge. Novel technologies for fighting cancer are expected to be developed with enhanced efficiency, decreased toxicity, and reversed drug multi-resistance. In recent years, photothermal therapy (PTT) has been gradually accepted for tumor therapy owning to its excellent effectiveness with minimal invasiveness and good compatibility [1,2]. Besides, it has also been used as an adjunct to pre-cancerous lesions and reduced residual tumor burden after post-surgical surgery [3,4]. It also can cooperate with traditional chemotherapy and radiotherapy in improving cancer treatment [5]. Under light irradiation, photothermal agents convert light energy into heat energy and increase the intratumoral temperature, leading to the death of cancer cells [6,7]. Thus, it is feasible to target the lesions directly, non-invasively to the surrounding healthy tissues.

It proves that the efficiency of PTT largely depends on the targeting capability of photothermal agents and their photothermal conversion efficiency [8]. The current research on photothermal therapy is focused on the rapidly-developing nanomaterials with great PTT potentials arising from the unique physiochemical properties of nanostructures including a strong optical absorption, an enhanced photothermal conversation efficiency, a controllable surface multi-functionalization, and the ability to deeply penetrating tissues [9]. Quite differently from the organic dyes with lower near-infrared (NIR) light absorption coefficient and severe photobleaching, nanomaterials have shown good performance as photothermal agents in PTT [10]. Many nanomaterials have been reported to have excellent performances as photothermal agents. Among them, metal-containing nanoparticles have attracted great attention for photothermal conversion owning to the excellent photothermal conversion ability and good biocompatibility [11]. In recent years, bismuth-based nanomaterials have been introduced as attractive theranostic agents due to their extraordinary thermoelectric, photoelectric and optical properties [12,13]. For instance, Bi_2Se_3 nanomaterials have been used to develop promising theranostics platforms for cancer therapy by virtue of their good safety profile, excellent X-ray CT imaging, photoacoustic imaging coupled with photothermal and photodynamic therapeutic effects [14]. The ultra-thin Bi_2Se_3 nanoparticles synthesized by Xie et al. were reported to produce a significant tumor photothermal effect with a good photothermal conversion capacity [15]. Macrophage membrane-camouflaged hollow Bi_2Se_3 nanoparticles loaded with quercetin were found to increase photothermal sensitivity and potently inhibit lung metastasis of breast cancer [16]. All of these reports have revealed the satisfactory performances of Bi_2Se_3 nanomaterials in PTT. However, the molecular mechanism underlying the photothermal effect of Bi_2Se_3 nanomaterials remains elusive and needs further exploration.

Autophagy, a self-degradative system, plays a vital role in maintaining cellular homeostasis [17]. It is usually considered as a self-defense mechanism and defends cells from various environmental insults and cellular stress such as heat, hypoxia, DNA damage, reactive oxygen species (ROS) and aggregation of misfolded proteins. Afterward, autophagy was found to be intimately implicated in cancer [18] and targeting autophagy has been regarded as a promising strategy for cancer treatment [19]. However, accumulating evidence has demonstrated that the effect of autophagy towards cancer may be sophisticated and depends on tumor type, development stage and tumor microenvironment [20]. Heat stress has been recognized as a trigger for autophagy [21] and even the involvement of autophagy in PTT effect has also been reported. Zhou and his colleagues found that autophagy inhibition could sensitize hyperthermia-induced killing of cancer cells [22]. Afterward, they found that beclin-1-induced autophagy up-regulation might destroy the homeostatic functions of autophagy and activate autophagy death pathways, thus improving the efficacy of photothermal killing [23].

Autophagy may affect apoptosis dependently on the type and state of the cell. Autophagy can contribute to pro-survival pathways, while inappropriate autophagy can cause cell death [24,25]. Autophagy could be regulated by cell stress-related signal paths, for instance, c-Jun N-terminal kinase (SAPK/JNK) [26] pathway and p38 MAP kinases (p38) pathway [27]. SAPK/JNK, a MAPK subfamily [28], generally induces apoptosis and growth inhibition in response to some stressors including UV irradiation and oxidative stress [29]. Many data have indicated that associations between JNK signaling and cancer [30]. Actually, JNK has been considered an attractive target for therapeutic intervention [31]. JNK activation can inhibit tumor formation and has a pro-apoptotic effect [32]. Similarly, p38 pathway is also activated responsive to various stresses and gets involved in different cell processes including autophagy [33] and cell death [34].

In this study, we plan to investigate the photothermal conversion capability as well as the photothermal killing effect of the synthesized Bi_2Se_3 nanoparticles. Emphasis may be put on the exploration of the involved biological mechanism including autophagy and stress-related signaling pathways (Figure 1a).

2. Materials and Methods

Dimethyl sulfoxide (DMSO), RPMI-1640 culture medium and phosphate buffer solution (PBS) were purchased from Hyclone (USA). Fetal bovine serum (FBS) and penicillin-streptomycin solution were purchased from Gibco (USA). Cell counting kit-8 (CCK-8) and calcein-AM/PI double stain kit were purchased from Dojindo Laboratories (Japan). All primary antibodies (LC3β, cleaved-PARP, p-p38, p-SAPK/JNK, p-Akt and GAPDH) and secondary antibody were purchased from Cell Signaling Technology (USA). ECL prime western blot detection reagent was purchased from GE Healthcare (USA). All aqueous solutions were prepared from a Milli-Q water system (Milli-Q, USA). A549 human lung adenocarcinoma cell line was obtained from ATCC.

2.1. Characterization of Bi_2Se_3 nanoparticles

Bi_2Se_3 nanoparticles were synthesized as described in the previous work of our group. In brief, to synthesize Bi_2Se_3 nanoparticles, 1.0 g of poly (vinylpyrrolidone) (PVP) dissolved in 19.5 mL of deionized water was heated to 80 ºC on a water bath under argon protection. Then 10 mL of L-selenocysteine dissolved in deionized water (3 mM) and 0.6 mL of NaOH (0.5 M) were slowly added to the flask and maintain the sample at 80 ºC for 10 min. Afterward, 0.5 mL of Bi $(NO_3)_3$ solution (0.1 M) was quickly added to the flask while vigorously stirring. The obtained solution was irradiated with visible light and kept at 80 ºC for 3 h. During this period, the solution's color gradually changed to brownish-black, indicating the formation of the product. As the reaction ended, the mixture was stood to cool to room temperature. The final product was washed three times with deionized water, dialyzed to further remove the impurities and finally stored at -20 ºC for use. Then the morphology, size and microstructures of synthesized Bi_2Se_3 nanoparticles were determined by a field emission scanning electron microscope (SEM, Hitachi S-4800, Japan) and a transmission electron microscope (TEM, Tecnai G2 F20 U-TWIN, USA). The elemental compositions of the nanoparticles were determined with an energy-dispersive spectrometer (EDS) attached to the SEM. Dynamic light scattering (DLS) analyzer (NanoBrook Omni) (Brookhaven Instruments, USA) was used to measure the hydrodynamic diameter and zeta potential of Bi_2Se_3 dispersion in purified water. Fourier Transform Infrared (FTIR) spectrometer (Thermo Scientific, USA) with Nicolet iN10 MX spectrograph was used to record the formation of PVP-Bi_2Se_3 in the powder form. To detect chemical structures of the formation of Bi_2Se_3, X-ray photoelectron spectroscopy (XPS, Thermo Scientific K-alpha) measurements were performed to characterize the chemical stoichiometry with monochromatic Al $K\alpha$ radiation (1486.6 eV). X-ray diffraction (XRD) patterns of the sample were performed by a Bruker D8 Advance X-ray diffractometer. The measurements were operated in the refection mode with Cu $K\alpha$ radiation, and the 2θ range between 5° and 80° were recorded.

2.2. Photothermal Conversion Performance of Bi_2Se_3 nanoparticles

UV-visible-near-infrared (UV-Vis-NIR) absorption spectra of Bi_2Se_3 with different concentrations (100, 200 μg/mL) were collected by UV-Vis spectrophotometer (UV 1800, Japan) with a wavelength coverage of 300-1000 nm. To further detect the photoabsorption capability, the extinction coefficient ε (λ) of the Bi_2Se_3 is calculated. Various concentrations of Bi_2Se_3 dispersions (0, 25, 50, 100 μg/mL) were irradiated with 808 nm laser (VLSM-808-B, China) (1.0 W/cm^2) for 10 min and temperatures were monitored by an infrared thermal imaging instrument (FLIR i7, USA). The photostability test was performed by irradiating Bi_2Se_3 dispersion with an 808 nm laser for 10 min and then turning off the laser for four cycles.

2.3. CCK-8 cell viability assay

A549 cells were cultivated in RPMI-1640 medium supplemented with 10% FBS, 1% penicillin/streptomycin at 37 ℃ in a 5% CO_2 and humid atmosphere. Changing the medium every 2 days and culture until cells are 80% confluence.

The cytotoxicity of Bi_2Se_3 nanoparticles was tested by CCK-8 assay. In detail, A549 cells were seeded into 96-well plates (1×10^4 cells/well) and cultured for 24 h until 80% confluence in a 37 ℃ incubator. Then changed the medium with a fresh medium containing different concentrations of Bi_2Se_3 (0, 6.25, 12.5, 25, 50, 100, 200 μg/mL) for 24 h. Cells were flushed twice with PBS followed by CCK-8 reagent incubation for 30 min at 37 ℃. Absorbance was measured in each well at 450 nm using a microplate reader (Victor X3, USA).

To explore the photothermal killing effect of Bi_2Se_3 nanoparticles, A549 cells were seeded into 96-well plates (1×10^4 cells/well) and cultured for 24 h. Then, cells were respectively incubated with 0, 6.25, 12.5, 25, 50, 100 and 200 μg/mL concentrations of Bi_2Se_3 nanoparticles in the absence or presence of laser irradiation. Irradiation was performed using an 808 nm laser with an intensity of 1.0 W/cm^2 and then cells were cultured for a further 12 h. Cell viability was tested using CCK-8 assay.

2.4. Live-Dead staining

Calcein-AM/propidium iodide staining was a routine method for assessing the status of cells based on membrane integrity. Calcein-AM and propidium iodide (PI) solutions can stain live and dead cells, respectively. Structurally, the high lipophilicity of methyl acetate helps calcein-AM penetrate live cells readily. AM group can be removed by active esterase in live cells, thus calcein emits strong green fluorescence. PI can only cross the cell membrane of dead cells where it embeds in DNA double helix and produces red fluorescence.

The well-grown cells were incubated with different concentrations of Bi_2Se_3 nanoparticles (0, 25, 50, 100, 200 μg/mL) in the absence or presence of laser irradiation. After 10 min of irradiation, cells were further cultured for 12 h and the treatment period ended. For calcein-AM/PI staining, cells were incubated with 2 μM calcein-AM and 2.5 μg/mL PI for 10 min at 37 °C. Representative images were obtained using a fluorescence inverted microscope system (Olympus IX81, Japan).

2.5. Annexin V-FITC/PI double labeling for apoptosis detection

Annexin V-FITC/PI apoptosis assay kit was used to evaluate the photothermal killing effect of Bi_2Se_3 nanoparticles. Well-grown cells were incubated with Bi_2Se_3 nanoparticles (0, 25, 50 μg/mL) and subject to laser irradiation for 10 min followed by a further incubation of 12 h. Then all the cells (both the attached and floating cells) were collected by trypsinization and centrifugation. The obtained cells were washed twice using PBS solution, resuspended in 500 μL of binding buffer containing 5 μL of annexin V- FITC and 5 μL of PI, then incubated for 15 min in the dark at room temperature. Apoptosis was immediately analyzed by flow cytometry (Accuri C6, USA).

2.6. Monodansylcadaverine (MDC) staining for autophagy assay

A549 cells were seeded on confocal dishes (1×10^4 cells/mL). After 24 h, cells were incubated with different concentrations of Bi_2Se_3 dispersions (0, 25, 50 μg/mL) for 6 h in the absence or presence of laser irradiation. At the end of exposure, cells were stained with 50 μM MDC for 20 min and Hoechst 33342 dye for 5 minutes in dark. Then samples were loaded onto a laser confocal microscope and the representative images were obtained.

2.7. Western blotting analysis

Western blotting analysis was performed as follows for total proteins. At the end of exposure, A549 cells were washed with ice-cold PBS solution and lysed in RIPA lysis buffer supplemented with complete protease inhibitor cocktails (Roche, Switzerland) on ice. The solutions of cytolysis were centrifuged (12 000 rpm) for 15 min at 4 ℃ and the supernatant liquor was collected into cold tubes. The total protein content of each sample was determined using a BCA protein detection kit (Applygen, China). 20 μg protein was loaded and separated on a 12% sodium dodecyl sulfate-polyacrylamide gel electrophoresis (SDS-PAGE) and transferred onto 0.22 μm polyvinylidene difluoride (PVDF) membrane. Immediately, PVDF membrane was washed three times with Tris-buffered saline

Tween-20 (1×TBST) and then blocked in 5% bovine serum albumin (BSA) for 1 h at room temperature. The membrane was incubated with the indicated primary antibodies including LC3β (1/3000), cleaved-PARP (1/4000), p-p38 (1/4000), p-SAPK/JNK (1/4000), p-Akt (1/4000) overnight at 4 °C. PVDF membranes were washed three times with 1×TBST and incubated with the corresponding peroxidase-conjugated secondary antibodies at room temperature for 1 h followed by three times of wash. Finally, target proteins were detected after incubation with an ECL reagent and immunoreactive bands were captured using a chemiluminescence imaging system (Azure C300, China). GAPDH was used as an internal reference. Band intensity on the exposed film was semi-quantified using ImageJ software (National Institutes of Health, Bethesda, Maryland, USA). All experiments were repeated at least three times independently.

2.8. Statistical analysis

All experiments in the current study were independently repeated at least 3 times with similar results. The relative percentage and values were presented as the Mean ± SD of six parallel samples. Statistical analysis was performed by two-tailed Student's t-test for unpaired data, with $p < 0.05$ considered statistically significant.

3. Results and discussions

3.1. Characterization of Bi_2Se_3 nanoparticles

Bi_2Se_3 nanoparticles were synthesized as described in *Methods and Materials*. Figure 1b shows the SEM images of the Bi_2Se_3 nanoparticles. The morphology of the synthesized Bi_2Se_3 was observed to be flower-like spherical in shape with a size of ~2.90 μm. Figure 1c shows the corresponding EDS results of the Bi_2Se_3 sample confirming the presence of Se and Bi. Typical transmission electron microscopy (TEM) images showed that the synthesized PVP-Bi_2Se_3 nanoparticles exhibited a relatively uniform nanostructure with an average diameter of ~2.75 μm (Figure 1d). The high-resolution TEM (HRTEM) image presented in Figure 1e, f demonstrated clear lattice fringes with 3.066 Å spacing corresponding to a lattice spacing of the (015) facets. The results from dynamic light scattering (DLS) analysis revealed that the average effective hydrated particle size of Bi_2Se_3 nanoparticles was approximately 2804.13 nm with good dispersion stability (Figure 1g), and their zeta potential was tested to be -32.61 mV. The characteristic peaks of L-selenocysteine include a broad-band at 2921 cm^{-1} assigned to the amino group stretching vibration, and the bands at 1401 and 1613 cm^{-1} corresponding to the symmetric and asymmetric flexural vibration of the carboxylic group, respectively (Figure 1h). Besides, the stretching bands of C-N are at 1120 and 1034 cm^{-1}, and the stretching band of C-Se is at 767 cm^{-1}. The above absorption bands are found in the spectrum of our synthesized Bi_2Se_3 nanoparticles, revealing the presence of L-selenocysteine on the surface of naked Bi_2Se_3. Besides, in the pure PVP spectrum, a very intense peak at 1647 cm^{-1} dues to carbonyl stretching of the five-membered cyclic lactam structure. The peaks at 2953 and 2876 cm^{-1} of spectrum related to C–H stretching for aliphatic compounds [35,36], of which the latter was found in the PVP-Bi_2Se_3. The band near 1278 cm^{-1} in the pure PVP spectrum due to the ring C-N stretching coupled with the ring CH_2 wagging [37], which could be observed in the PVP- Bi_2Se_3 sample FTIR spectrum. It proved that PVP was coated on the surface of Bi_2Se_3. The typical XPS survey scan spectrum of synthesized Bi_2Se_3 shows the presence of Bi, Se, and N elements in the sample (Figure 1i). Figure 1j and Figure 1k show the high-resolution XPS (HR-XPS) spectra of Bi 4f and Se 3d, respectively. As the Bi 4f spectrum shown (Figure 1j), the binding energies at 158.4 and 163.7 eV are assigned to Bi $4f_{7/2}$ and Bi $4f_{5/2}$, respectively. The peaks at 54.3 and 55.2 eV are corresponding to Se $3d_{5/2}$ and Se $3d_{3/2}$, respectively, which are consistent with the reported XPS data of Bi_2Se_3 [38–40]. Figure 1k also showed shoulders at 58.1 eV, which resulted from the formation of Se-O bonds, suggesting the oxidation of Bi_2Se_3 [39,41], and the oxidation has been reported to be commonly present in Bi_2Se_3 nanoparticle [41]. XPS results further confirmed the synthesized Bi_2Se_3 nanoparticles, and the Bi and Se atoms of Bi_2Se_3 are in the valence state of -2 and +3, respectively. Figure 1l shows XRD patterns of Bi_2Se_3 determine a very strong (015) orientation peak, which is consistent with the plane orientation of Bi_2Se_3 in HRTEM result (see figure 1f). The strong diffraction peaks can be indexed as the layered rhombohedral phase of Bi_2Se_3 (JCPDS Card No. 33-0214). The well-defined peaks verify the forming of high-quality Bi_2Se_3.

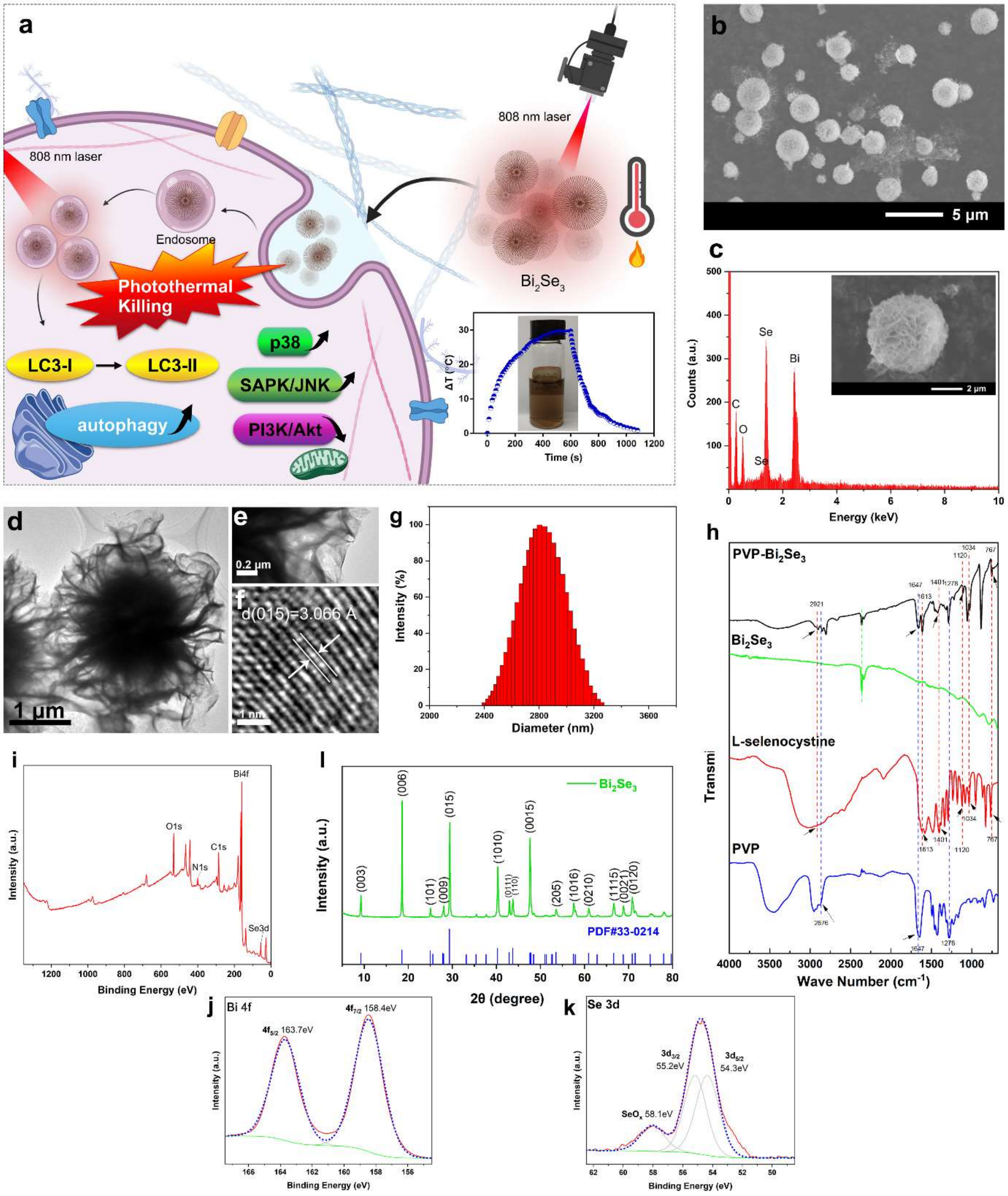

Figure 1. Physicochemical characterizations of Bi_2Se_3 nanoparticles. (**a**) Schematic shows the synthesized Bi_2Se_3 nanoparticles performed a remarkable photothermal killing of A549 cells via apoptosis mechanism; (**b**) SEM image of the PVP- Bi_2Se_3 nanoparticles; (**c**) EDS spectrum of Bi_2Se_3. The inset shows a high-magnification SEM image of Bi_2Se_3 nanoparticles; (**d**) TEM image of the synthesized Bi_2Se_3 nanoparticles; (**e**) and (**f**) Magnified TEM image; (**g**) The size distribution of Bi_2Se_3 nanoparticles dispersed in water; (**h**) FTIR spectra of PVP-Bi_2Se_3, Bi_2Se_3, L-selenocysteine and PVP; (**i**) Survey scan XPS spectrum of the Bi_2Se_3 nanoparticles; HR-XPS spectra of (**j**) Bi 4f and (**k**) Se 3d scans of Bi_2Se_3 nanoparticles. The solid lines represent the data curves, while the dot lines are the fitted curves; (**l**) XRD patterns of Bi_2Se_3 nanoparticles.

3.2. Photothermal profile of Bi_2Se_3 nanoparticles

Bi_2Se_3 powder was dispersed in water and the obtained dispersion was brown-black optically. The UV-visible-NIR absorption spectra of Bi_2Se_3 dispersion displayed a certain absorption in the NIR region, suggesting its potential photothermal efficacy (Figure 2a). The molar extinction coefficient ε_{808} of the Bi_2Se_3 nanoparticles was calculated from the measured absorbance in equation (1) [42,43],

$$\varepsilon_{808} = (\mathrm{A}_{808}\mathrm{V}\rho\mathrm{N}_A)/(LC) \tag{1}$$

where A is the absorbance of the Bi_2Se_3 nanoparticles at 808 nm wavelength (Figure 2a), V (unit: cm^3) is the average volume of individual Bi_2Se_3 nanoparticle, and ρ is the density of the Bi_2Se_3 nanoparticle (7.51 g/cm^3) [44]. N_A is Avogadro's constant, L is the path-length (unit: cm), and C (unit: g/L) is the weight concentration of the Bi_2Se_3 dispersion. The result demonstrated that the Bi_2Se_3 nanoparticles had a high ε with ~1.7×10^{13} $M^{-1}\cdot cm^{-1}$ at 808 nm (100 μg/mL) (Figure 2b). Besides, to directly evaluate the photothermal conversion capacity of Bi_2Se_3 nanoparticles, their thermal performance was monitored during laser irradiation of 10 min (Figure 2**c**). The temperatures of Bi_2Se_3 dispersions were tested to time- and concentration-dependently increase under laser irradiation and finally reached a platform, quite differently from the subtle change in the temperature of pure water upon irradiation. The temperature of 100 μg/mL Bi_2Se_3 dispersion sharply increased to 56.3 °C under laser irradiation (1.0 W/cm^2), indicating that the synthesized Bi_2Se_3 can efficiently convert 808 nm NIR energy into heat energy. To obtain the heat conversion efficiency (η) of Bi_2Se_3 dispersions (100 μg/mL), we kept a record of temperature difference (ΔT) under the 808 nm laser (1.0 W/cm^2). Until the temperature stops rising, the irradiation source was shut off. The temperature decline was monitored (Figure 2d). According to the obtained data, we plotted the linear time data and negative values of the natural logarithm of driving force temperature obtained from cooling period (after 600 s) (Figure 2e). The time constant for heat transfer is calculated to be τ_s=142.6 s. Then, η_{808} was calculated by equation (2) [43,45,46]:

$$\eta_{808} = \frac{\hbar S\Delta T_{max} - Qs}{I(1 - 10^{-A_{808}})} \tag{2}$$

where ΔT_{max} is the maximum stable state temperature (29.67 °C), Q_S is the baseline energy input of deionized water, which is determined independently to be 0.005 mW. I is the laser power, 1.0 W/cm^2. A_{808} is the absorbance at 808 nm (0.15, Figure 2a), and hS is obtained via equation (3) [47].

$$hS = \frac{mC}{\tau_s} \tag{3}$$

where m is the mass (g) of deionized water, C is heat capacity under constant pressure (J/g·°C). Substituting hS into equation (2), η_{808} of Bi_2Se_3 can reach ~28.95 %. This result exhibited a remarkable photothermal conversion capacity possessed by the synthesized Bi_2Se_3 nanoparticles. Then, we chose 50 μg/mL Bi_2Se_3 dispersion for the photostability test. We irradiated Bi_2Se_3 dispersion for 10 min for four cycles separated by 10 min closure of irradiation to allow the temperature recovery, during which the alterations in temperature were carefully monitored. The results demonstrated that the photothermal conversion capacity was still maintained after four continuous heating and cooling cycles of Bi_2Se_3 nanoparticles, suggesting good photostability (Figure 2f). Herein, the physicochemical properties of Bi_2Se_3 suggested it promising as a prominent photothermal agent.

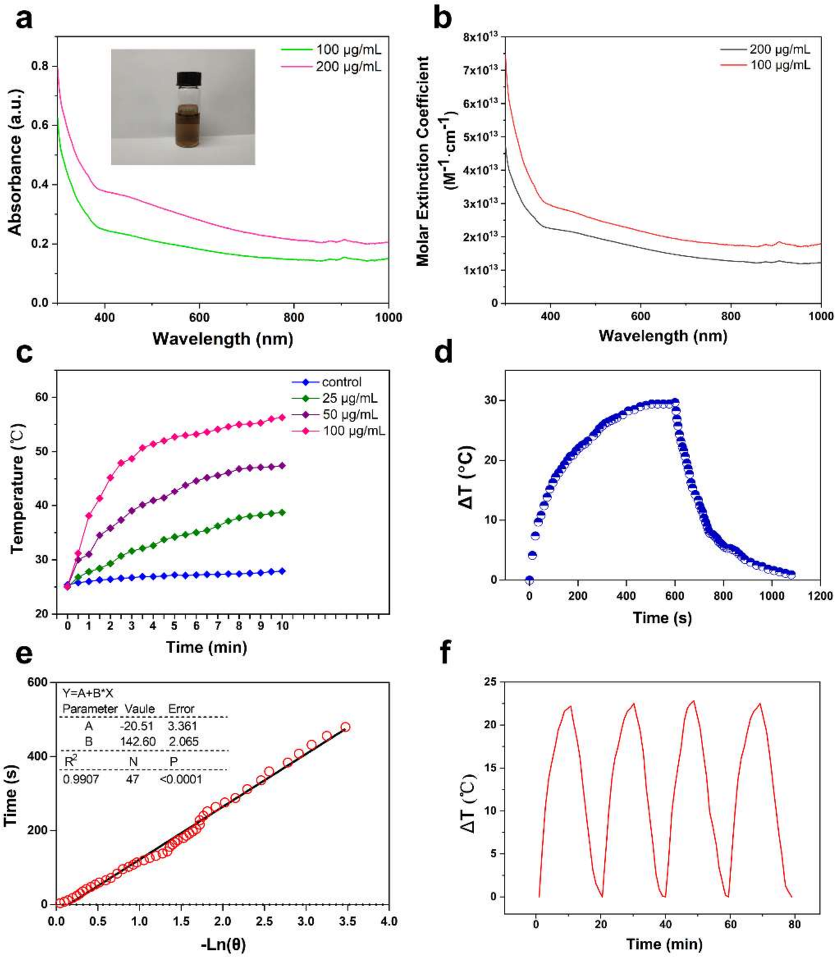

Figure 2. Photothermal profile of Bi_2Se_3 nanoparticles. (**a**) Room-temperature UV–Vis-NIR absorbance spectra for the Bi_2Se_3 dispersed in deionized water with 100 and 200 μg/mL concentrations. Inset of the photo showing 100 μg/mL Bi_2Se_3 dispersion; (**b**) ε of Bi_2Se_3 nanoparticles (100 and 200 μg/mL); (**c**) Temperature elevation curve of Bi_2Se_3 dispersion under 808 nm laser (1.0 W/cm^2); (**d**) Photothermal effect of the irradiation of Bi_2Se_3 dispersion (100 μg/mL) with the NIR laser (808 nm, 1.0 W/cm^2). The laser was removed after irradiation for 600 s; (**e**) A linear graph of time and the negative natural logarithm of driving force temperature obtained from the cooling period (after 600 s) of Figure 2d; (**f**) Photostability test curve of Bi_2Se_3 nanoparticles at the concentration of 50 μg/mL within four laser on/off cycles (1.0 W/cm^2).

3.3. The photothermal effect of Bi_2Se_3 nanoparticles

It is crucial to assess the cytotoxicity of Bi_2Se_3 nanoparticles when considering the potential applications in the biomedical field. Herein, A549 cells were incubated with various concentrations of Bi_2Se_3 dispersions ranging from 0 to 200 μg/mL and cell viability was explored using CCK-8 assay after 24 h. The results demonstrated that Bi_2Se_3 was non-toxic to A549 cells, even at concentrations up to 200 μg/mL (Figure 3a). To investigate the photothermal killing of cancer cells by Bi_2Se_3 nanoparticles, Bi_2Se_3-incubated A549 cells were irradiated with 808 nm laser for 10 min and then incubated for a further 12 h without irradiation. The results from cell viability analysis demonstrated that under laser irradiation, Bi_2Se_3 nanoparticles induced a concentration-dependent decrease in the viability of A549 cells. Under laser irradiation, the viability of cells incubated with 12.5 μg/mL Bi_2Se_3 dispersion was approximately 80% of the control cells while the cell viability decreased to 25% as the concentration of Bi_2Se_3 increased to 200 μg/mL (Figure 3b). Instead, neither only laser irradiation nor only Bi_2Se_3 exposure decreased cell viability. Herein, it showed that both laser irradiation and Bi_2Se_3 nanoparticles were required for the killing of cancer cells, suggesting a photothermal killing of cancer cells by Bi_2Se_3 nanoparticles. Calcein-AM/PI live-dead staining further confirmed the photothermal killing of Bi_2Se_3 nanoparticles. It showed that only green fluorescence existed in the cells incubated with either Bi_2Se_3 nanoparticles or irradiation, indicating that no cytotoxicity was induced by laser irradiation only or nanoparticles only. In Bi_2Se_3-exposed cells upon NIR light irradiation appeared the red fluorescence, revealing the photothermal cell death induced by Bi_2Se_3 nanoparticles. Moreover, with laser irradiation, more red fluorescent spots were observed in cells incubated with 200 μg/mL Bi_2Se_3 dispersion than that incubated with 100 μg/mL Bi_2Se_3 dispersion, exhibiting a concentration-dependent photothermal killing of Bi_2Se_3 nanoparticles (Figure 3c). This result was highly consistent with the result from the CCK-8 assay, together demonstrating a potent photothermal killing ability of Bi_2Se_3 nanoparticles advantageous for cancer therapy.

The photothermal killing of A549 cells by Bi_2Se_3 nanoparticles was further confirmed using Annexin V-FITC/PI double labeling kit. The results from flow cytometry analysis demonstrated that the apoptosis rate of Bi_2Se_3-exposed cells combined with laser irradiation is significantly higher than that of irradiation only group or Bi_2Se_3 exposure group only. The apoptosis-inducing effect of Bi_2Se_3 exposure plus laser irradiation was also shown to be concentration-dependent (Figure 3d). The percentage of apoptotic cells in each group was quantified in Figure 3e.

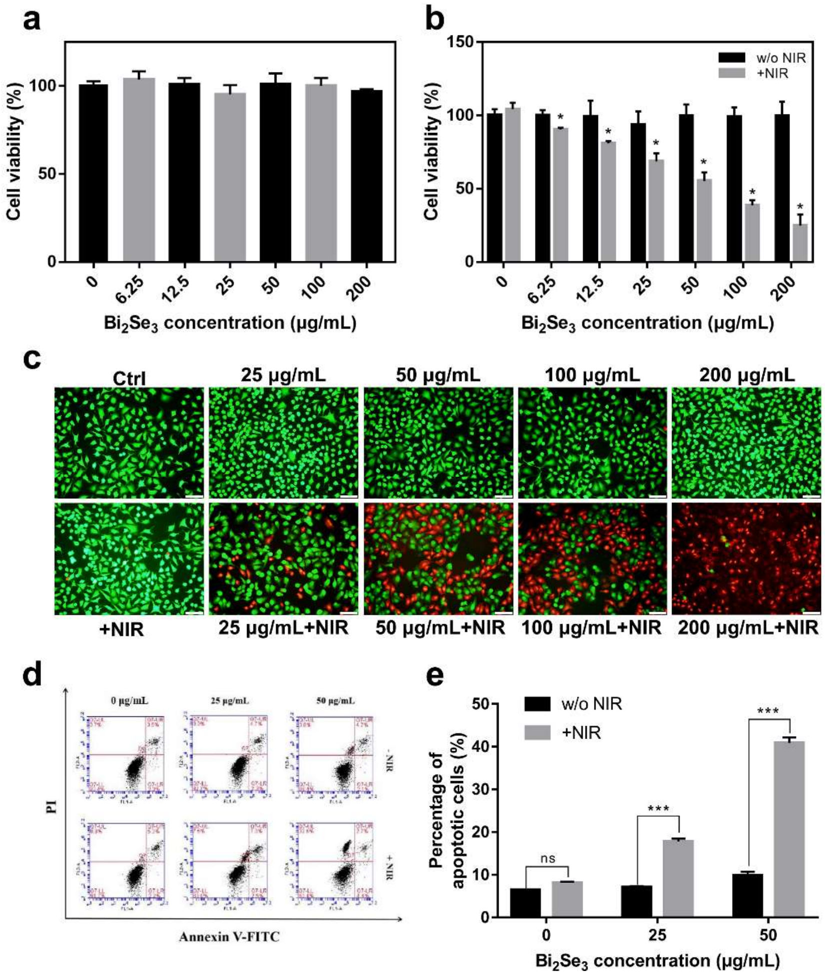

Figure 3. Photothermal killing of A549 cells by Bi_2Se_3 nanoparticles. (**a**) Relative viability of A549 cells incubated with diverse concentrations of Bi_2Se_3 nanoparticles (0, 6.25, 12.5, 25, 50, 100, 200

μg/mL) for 24 h; (**b**) The cell viability of A549 cells upon Bi_2Se_3 exposure (0, 6.25, 12.5, 25, 50, 100, 200 μg/mL) with or w/o laser irradiation. **p* < 0.05, versus untreated control group; (**c**) Live-dead staining fluorescence images of A549 cells. A549 cells were incubated with Bi_2Se_3 nanoparticles with or w/o laser irradiation. Cells with green fluorescence (calcein-positive cells) represent live cells while red fluorescence dead cells (PI-positive cells). Scale bar: 40 μm. The demonstrated images are the representatives of three independent experiments; (**d**) Apoptosis analysis by flow cytometry using Annexin V-FITC/PI staining kit. Cells were incubated with Bi_2Se_3 nanoparticles (0, 25, 50 μg/mL) and subject to laser irradiation for 10 min followed by a further incubation of 12 h. Then cells were harvested for apoptosis detection after annexin V-FITC/PI staining. Representative flow cytometry data were presented; (**e**) The apoptotic rates of each group from the results of three independent experiments were quantified (****p* < 0.001).

3.4. Autophagy involved in photothermal killing of Bi_2Se_3 nanoparticles

In advance to high temperature-induced cell death, autophagy is probably triggered to cope with harsh environments and cellular stress [48]. To explore whether autophagy was involved in the photothermal killing effect of Bi_2Se_3 nanoparticles, autophagosome formation was observed first using MDC staining. The results demonstrated that autophagy was induced in Bi_2Se_3-incubated cells upon laser irradiation. The intracellular bright green fluorescence illustrated that there were autophagosomes in cytoplasm of A549 cells [49]. A slight green fluorescence was present in control cells with neither Bi_2Se_3 incubation nor laser irradiation. Laser irradiation itself also failed to trigger autophagy as no obvious green fluorescence was observed in the cytoplasm of only irradiated cells. Also, no obvious autophagy was induced in Bi_2Se_3-incubated cells with no irradiation. Distinctly, a significant increase in the fluorescence intensity representing autophagosome formation was observed in Bi_2Se_3-incubated cells upon laser irradiation, demonstrating autophagy induction by the photothermal role of Bi_2Se_3 nanoparticles (Figure 4a). Furthermore, upon laser irradiation, a higher concentration of Bi_2Se_3 exposure triggered more potent autophagy in cells. Then the green fluorescence intensity in each group of A549 cells was quantified by ImageJ software and presented in Figure 4b.

When autophagy occurs, partial cellular components are encapsulated in autophagosomes and eventually degraded on fusion with lysosomes. Microtubule-associated protein 1 light chain 3 (LC3) is a signature protein of autophagy composed of cytoplasmic LC3 (LC3-I) and LC3-II spotted on the membrane of autophagosomes [50]. The conversion of LC3 protein from LC3-I to LC3-II is widely recognized as an indicator of autophagy behavior [51]. Autophagy induced by the photothermal effect of Bi_2Se_3 nanoparticles was also confirmed by an increased ratio of LC3-II / LC3-I. The results from western blotting analysis demonstrated that the abundance of LC3-II was increased obviously in Bi_2Se_3-exposed cells upon laser irradiation, especially in the group of 50 μg/mL Bi_2Se_3 dispersion (Figure 4c). It should be pointed out that the total expression of LC3 protein (both LC3-I and LC3-II) in the irradiated cells incubated with 100 μg/mL Bi_2Se_3 displayed a lower level, which was inferred to be related to the acceleration of autophagy protein degradation at the high concentration. Compared with other groups, the ratio of LC3-II/I in Bi_2Se_3-exposed cells combined with laser irradiation was significantly higher (Figure 4d), indicating an enhanced autophagy level. Therefore, it confirmed that Bi_2Se_3 nanoparticles could induce autophagy in A549 cells under laser irradiation.

Then, we investigated the effect of 3-methyladenine (3-MA), a specific autophagy inhibitor, on the photothermal killing of Bi_2Se_3 nanoparticles *in vitro*. 3-MA with concentrations of less than 2.5 mM has marginal effects on the viability of A549 cells (Figure 4e). Notably, 1 h pretreatment of 1 mM 3-MA obviously increased the photothermal killing capability of Bi_2Se_3 nanoparticles as seen from the further decrease in cell viability by 3-MA pretreatment (Figure 4f). The results suggested that autophagy inhibition might enable a more efficient photothermal killing of Bi_2Se_3 nanoparticles.

To summarize, autophagy was enhanced in A549 cells by Bi_2Se_3 nanoparticles upon laser irradiation and autophagy inhibition by 3-MA probably enabled a more efficient photothermal killing of Bi_2Se_3 nanoparticles.

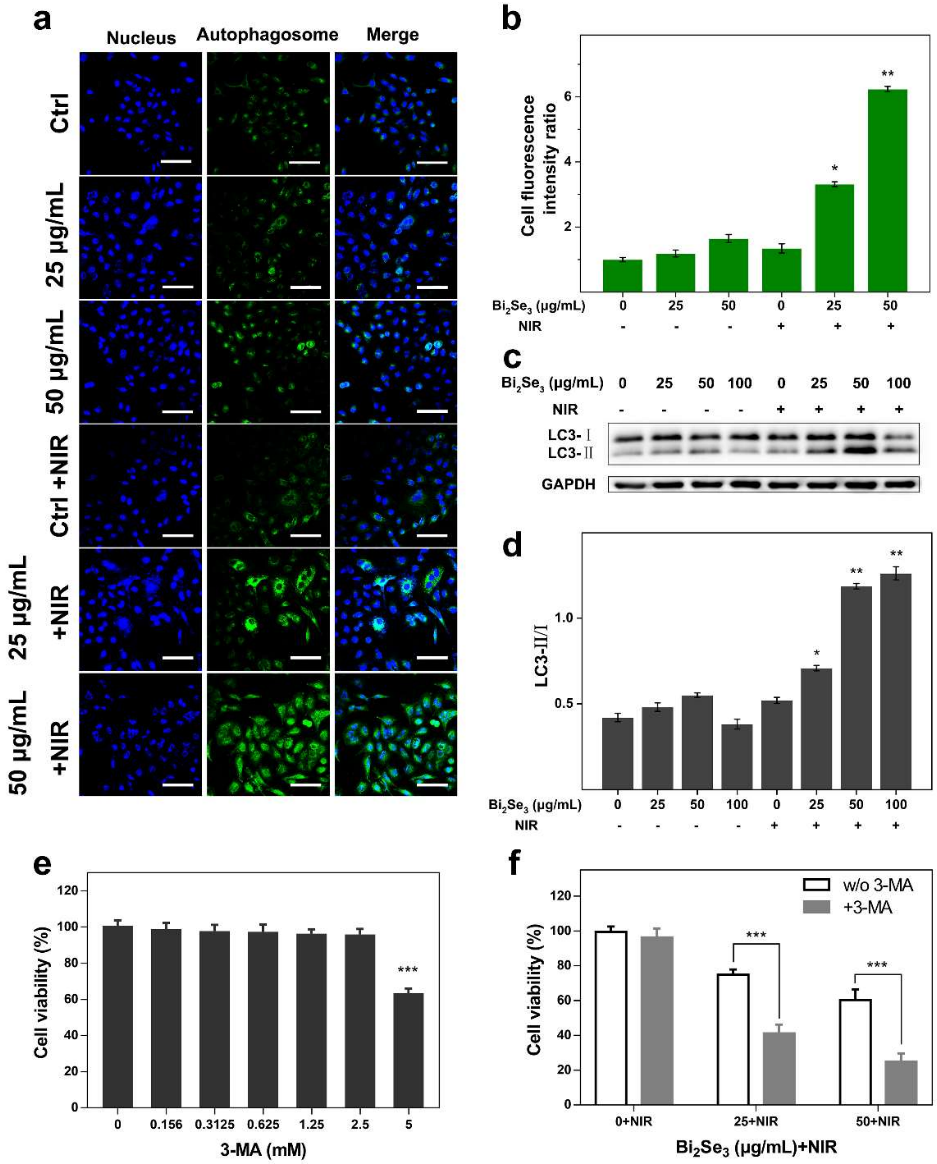

Figure 4. Autophagy induced by Bi_2Se_3 nanoparticles upon laser irradiation. (**a**) Autophagosome formation in Bi_2Se_3-incubated cells upon irradiation as observed by MDC staining. A549 cells were treated with diverse concentrations of Bi_2Se_3 nanoparticles (0, 25, 50 μg/mL) with or without laser irradiation. The nucleus was stained with Hoechst 33342 (blue) and autophagic vacuole was stained with MDC (green). Representative images were obtained using confocal fluorescence microscopy. Scale bar: 80 μm; (**b**) The mean fluorescence intensity of MDC dye in each group of A549 cells of 10 different fields was quantified using ImageJ. $^{*}p < 0.05$, $^{**}p < 0.01$ versus control group (irradiated cells without Bi_2Se_3 incubation); (**c**) The increased LC3 II/I level in Bi_2Se_3-exposed cells upon laser irradiation. Cells were exposed to diverse concentrations of Bi_2Se_3 nanoparticles (0, 25, 50, 100 μg/mL) with or without irradiation. The molecular weight of LC3-I (cytosolic form) is 16 KD and the molecular weight of LC3-II (bound form) is 14 KD. GAPDH serves as a loading protein. The representative data of three independent experiments were shown here; (**d**) The relative expressions of LC3 II /I in each group from the results of three independent experiments were quantified using ImageJ ($^{*}p < 0.05$, $^{**}p < 0.01$); (**e**) The effect of 3-MA on the basal cell viability of A549 cells; (**f**) The effect of 3-MA on the photodynamic killing of Bi_2Se_3 nanoparticles. 3-MA might strengthen the photodynamic killing effect of Bi_2Se_3 nanoparticles. The data presented are representative of three independent experiments ($^{***}p < 0.001$).

3.5. Activated stress-related p38 and SAPK/JNK signaling pathways coupled with the attenuated PI3K/Akt signaling in the photothermal effect of Bi_2Se_3 nanoparticles

As demonstrated above, upon laser irradiation, Bi_2Se_3 nanoparticles induced a photothermal killing of cancer cells. In response to the hyperthermal stimuli, the intracellular stress-related signaling pathways including p38 and p-SAPK/JNK are usually initiated. Using western blot analysis, the phosphorylation levels of p38 and p-SAPK/JNK were detected to be increased in Bi_2Se_3-incubated cells upon irradiation. Especially in the irradiated cells incubated with 50 μg/mL Bi_2Se_3 nanoparticles, the phosphorylation levels of p38 and p-SAPK/JNK were dramatically increased, suggesting potent activations of p38 and p-SAPK/JNK signaling pathways. Accordingly, the expression level of cleaved-PARP, an apoptotic marker, was elevated obviously in the group of 50 μg/mL Bi_2Se_3-incubated cells upon irradiation (Figure 5a), consistently with the results from CCK-8 and live-dead staining. As expected, PI3K/Akt signaling, which generally associates with cell survival and growth[52], was significantly attenuated in Bi_2Se_3-exposed cells upon irradiation. The phosphorylation level of Akt in Bi_2Se_3-exposed cells combined with irradiation was significantly reduced (Figure 5a). The results were quantified by ImageJ and demonstrated in Figure 6b that pointed out the increased levels of cleaved-PARP, phosphorylated p38 and p-SAPK/JNK as well as the decreased level of phosphorylated Akt in cells with Bi_2Se_3 incubation plus laser irradiation. Herein, the activated stress-related SAPK/JNK and p38 signaling pathways coupled with the attenuated PI3K/Akt signaling were involved in the photothermal killing effect of Bi_2Se_3 nanoparticles.

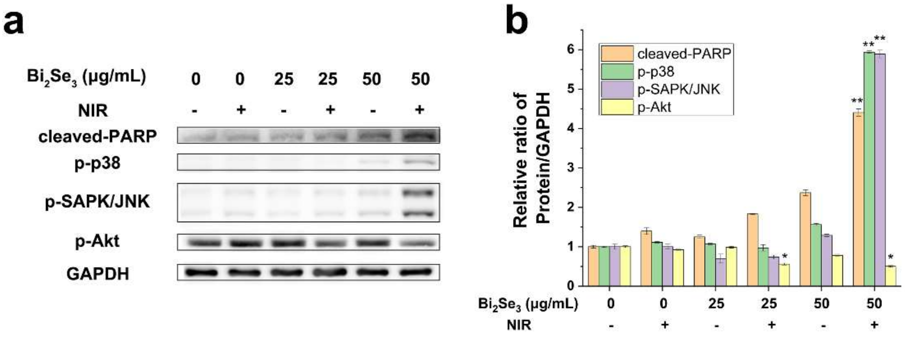

Figure 5. Effects of Bi_2Se_3 nanoparticles on intracellular stress-related and survival-associated signaling pathways. (**a**) The expressions of cleaved-PARP, phosphorylated p38 (p-p38), phosphorylated SAPK/JNK (p-SAPK/JNK) and phosphorylated Akt (p-Akt) in A549 cells under different conditions were obtained by western blot analysis. GAPDH serves as a loading protein. The representative data of three independent experiments were shown here; (**b**) The bands of these proteins of interest proteins from the results of three independent experiments were quantified using ImageJ. $^*p < 0.05$, $^{**}p < 0.01$ versus control group. The data presented are representative of three independent experiments.

4. Conclusions

In the present work, the synthesized Bi_2Se_3 nanoparticles exhibited good biocompatibility, excellent photothermal conversion capability and photostability. With laser irradiation, Bi_2Se_3 nanoparticles performed a significant photothermal killing of A549 cells via apoptosis mechanism. Moreover, autophagy induction was involved in the effect of Bi_2Se_3 nanoparticles which may be a self-protective behavior against the hyperthermal stimuli as inferred from a more severe cell death triggered by the pretreatment of 3-MA. Autophagy inhibition by 3-MA probably enabled a more efficient photothermal therapy. Simultaneously, stress-related p38 and p-SAPK/JNK signaling pathways were obviously activated accompanied by the attenuated PI3K/Akt signaling. Our work provides new insight into the mechanism underlying the photothermal effects of Bi_2Se_3 nanoparticles.

Author Contributions: Conceptualization, Yue You, Jinxia Li, Xinghua Dong and Feng Zhao; Formal analysis, Linlin Chen; Funding acquisition, Feng Zhao; Investigation, Yue You, Linlin Chen and Xinghua Dong; Methodology, Yue You, Jinxia Li, Linlin Chen, Mei Wang, Xinghua Dong, Liang Yan and Aiping Zhang; Project administration, Feng Zhao; Software, Yue You and Linlin Chen; Supervision, Feng Zhao; Visualization, Jinxia Li, Mei Wang, Liang Yan and Aiping Zhang; Writing – original draft, Yue You, Jinxia Li and Linlin Chen; Writing – review & editing, Yue You, Jinxia Li and Feng Zhao.

Funding: This research was funded by NSFC, grant number 21301176, 11305182.

Acknowledgments: This work was financially supported by NSFC (21301176, 11305182), the Science and Technology Innovation Project of IHEP (Y954513).

Conflicts of Interest: The authors declare no conflict of interest.

References

1. Shao, J.; Xie, H.; Huang, H.; Li, Z.; Sun, Z.; Xu, Y.; Xiao, Q.; Yu, X.-F.; Zhao, Y.; Zhang, H.; et al. Biodegradable Black Phosphorus-Based Nanospheres for in Vivo Photothermal Cancer Therapy. *Nat. Commun.* **2016**, *7*, 12967, doi:10.1038/ncomms12967.
2. Li, X.; Lovell, J.F.; Yoon, J.; Chen, X. Clinical Development and Potential of Photothermal and Photodynamic Therapies for Cancer. *Nat. Rev. Clin. Oncol.* **2020**, *17*, 657–674, doi:10.1038/s41571-020-0410-2.
3. Chen, Q.; Xu, L.; Liang, C.; Wang, C.; Peng, R.; Liu, Z. Photothermal Therapy with Immune-Adjuvant Nanoparticles Together with Checkpoint Blockade for Effective Cancer Immunotherapy. *Nat. Commun.* **2016**, *7*, 13193, doi:10.1038/ncomms13193.
4. Wang, Y.-T.; Lu, X.-M.; Zhu, F.; Huang, P.; Yu, Y.; Zeng, L.; Long, Z.-Y.; Wu, Y.-M. The Use of a Gold Nanoparticle-Based Adjuvant to Improve the Therapeutic Efficacy of HNgR-Fc Protein Immunization in Spinal Cord-Injured Rats. *Biomaterials* **2011**, *32*, 7988–7998, doi:https://doi.org/10.1016/j.biomaterials.2011.07.009.
5. Li, Z.H.; Chen, Y.J.; Yang, Y.; Yu, Y.; Zhang, Y.H.; Zhu, D.H.; Yu, X.P.; Ouyang, X.X.; Xie, Z.Y.; Zhao, Y.L.; et al. Recent Advances in Nanomaterials-Based Chemo-Photothermal Combination Therapy for Improving Cancer Treatment. *Front. Bioeng. Biotechnol.* **2019**, *7*, doi:ARTN 29310.3389/fbioe.2019.00293.
6. Shanmugam, V.; Selvakumar, S.; Yeh, C.S. Near-Infrared Light-Responsive Nanomaterials in Cancer Therapeutics. *Chem. Soc. Rev.* **2014**, *43*, 6254–6287, doi:10.1039/c4cs00011k.
7. Hildebrandt, B.; Wust, P.; Ahlers, O.; Dieing, A.; Sreenivasa, G.; Kerner, T.; Felix, R.; Riess, H. The Cellular and Molecular Basis of Hyperthermia. *Crit. Rev. Oncol. Hematol.* **2002**, *43*, 33–56, doi:Pii S1040-8428(01)00179-2Doi 10.1016/S1040-8428(01)00179-2.
8. Tan, L.J.; Wu, Z.Y.; Wang, X.J.; Sun, J. Facile Synthesis of CuS Mesostructures with High Photothermal Conversion Efficiency (Vol 5, Gp 35317, 2015). *Rsc Adv.* **2015**, *5*, 39192, doi:10.1039/c5ra90042e.
9. Chen, J.Q.; Ning, C.Y.; Zhou, Z.N.; Yu, P.; Zhu, Y.; Tan, G.X.; Mao, C.B. Nanomaterials as Photothermal Therapeutic Agents. *Prog. Mater. Sci.* **2019**, *99*, 1–26, doi:10.1016/j.pmatsci.2018.07.005.
10. Shibu, E.S.; Hamada, M.; Murase, N.; Biju, V. Nanomaterials Formulations for Photothermal and Photodynamic Therapy of Cancer. *J. Photochem. Photobiol. C-Photochemistry Rev.* **2013**, *15*, 53–72, doi:10.1016/j.jphotochemrev.2012.09.004.
11. Vines, J.B.; Yoon, J.H.; Ryu, N.E.; Lim, D.J.; Park, H. Gold Nanoparticles for Photothermal Cancer Therapy. *Front. Chem.* **2019**, *7*, doi:ARTN 16710.3389/fchem.2019.00167.
12. Cheng, X.J.; Yong, Y.; Dai, Y.H.; Song, X.; Yang, G.; Pan, Y.; Ge, C.C. Enhanced Radiotherapy Using Bismuth Sulfide Nanoagents Combined with Photo-Thermal Treatment. *Theranostics* **2017**, *7*, 4087–4098, doi:10.7150/thno.20548.
13. Wang, L.P.; Long, N.J.; Li, L.H.; Lu, Y.; Li, M.; Cao, J.K.; Zhang, Y.; Zhang, Q.Y.; Xu, S.H.; Yang, Z.M.; et al. Multi-Functional Bismuth-Doped Bioglasses: Combining Bioactivity and Photothermal Response for Bone Tumor Treatment and Tissue Repair (Vol 7, 1, 2018). *Light. Appl.* **2019**, *8*, doi:ARTN 5410.1038/s41377-019-0165-7.
14. Li, J.; Jiang, F.; Yang, B.; Song, X.R.; Liu, Y.; Yang, H.H.; Cao, D.R.; Shi, W.R.; Chen, G.N. Topological Insulator Bismuth Selenide as a Theranostic Platform for Simultaneous Cancer Imaging and Therapy. *Sci. Rep.* **2013**, *3*, doi:ARTN 199810.1038/srep01998.
15. Xie, H.H.; Li, Z.B.; Sun, Z.B.; Shao, J.D.; Yu, X.F.; Guo, Z.N.; Wang, J.H.; Xiao, Q.L.; Wang, H.Y.; Wang, Q.Q.; et al. Metabolizable Ultrathin Bi2Se3 Nanosheets in Imaging-Guided Photothermal Therapy. *Small* **2016**, *12*, 4136–4145, doi:10.1002/smll.201601050.
16. Zhao, H.J.; Li, L.; Zhang, J.L.; Zheng, C.X.; Ding, K.L.; Xiao, H.F.; Wang, L.; Zhang, Z.Z. C-C Chemokine Ligand 2 (CCL2) Recruits Macrophage-Membrane-Camouflaged Hollow Bismuth Selenide Nanoparticles To Facilitate Photothermal Sensitivity and Inhibit Lung Metastasis of Breast Cancer. *ACS Appl. Mater. Interfaces* **2018**, *10*, 31124–31135, doi:10.1021/acsami.8b11645.
17. Lee, J.; Giordano, S.; Zhang, J.H. Autophagy, Mitochondria and Oxidative Stress: Cross-Talk and Redox Signalling. *Biochem. J.* **2012**, *441*, 523–540, doi:10.1042/Bj20111451.
18. Galluzzi, L.; Pietrocola, F.; Bravo-San Pedro, J.M.; Amaravadi, R.K.; Baehrecke, E.H.; Cecconi, F.; Codogno, P.; Debnath, J.; Gewirtz, D.A.; Karantza, V.; et al. Autophagy in Malignant Transformation and Cancer Progression. *Embo J.* **2015**, *34*, 856–880, doi:10.15252/embj.201490784.

19. Galluzzi, L.; Bravo-San Pedro, J.M.; Levine, B.; Green, D.R.; Kroemer, G. Pharmacological Modulation of Autophagy: Therapeutic Potential and Persisting Obstacles. *Nat. Rev. Drug Discov.* **2017**, *16*, 487–511, doi:10.1038/nrd.2017.22.
20. Levy, J.M.M.; Towers, C.G.; Thorburn, A. Targeting Autophagy in Cancer. *Nat. Rev. Cancer* **2017**, *17*, 528–542, doi:10.1038/nrc.2017.53.
21. Hale, B.J.; Hager, C.L.; Seibert, J.T.; Selsby, J.T.; Baumgard, L.H.; Keating, A.F.; Ross, J.W. Heat Stress Induces Autophagy in Pig Ovaries during Follicular Development. *Biol. Reprod.* **2017**, *97*, 426–437, doi:10.1093/biolre/iox097.
22. Zhou, Z.J.; Yan, Y.; Hu, K.W.; Zou, Y.; Li, Y.W.; Ma, R.; Zhang, Q.; Cheng, Y.Y. Autophagy Inhibition Enabled Efficient Photothermal Therapy at a Mild Temperature. *Biomaterials* **2017**, *141*, 116–124, doi:10.1016/j.biomaterials.2017.06.030.
23. Zhou, Z.J.; Yan, Y.; Wang, L.; Zhang, Q.; Cheng, Y.Y. Melanin-like Nanoparticles Decorated with an Autophagy-Inducing Peptide for Efficient Targeted Photothermal Therapy. *Biomaterials* **2019**, *203*, 63–72, doi:10.1016/j.biomaterials.2019.02.023.
24. D'Arcy, M.S. Cell Death: A Review of the Major Forms of Apoptosis, Necrosis and Autophagy. *Cell Biol Int* **2019**, *43*, 582–592, doi:10.1002/cbin.11137.
25. Maiuri, M.C.; Zalckvar, E.; Kimchi, A.; Kroemer, G. Self-Eating and Self-Killing: Crosstalk between Autophagy and Apoptosis. *Nat. Rev. Mol. Cell Biol.* **2007**, *8*, 741–752, doi:10.1038/nrm2239.
26. Zhou, Y.Y.; Li, Y.; Jiang, W.Q.; Zhou, L.F. MAPK/JNK Signalling: A Potential Autophagy Regulation Pathway. *Biosci Rep* **2015**, *35*, doi:10.1042/BSR20140141.
27. Zhong, W.; Zhu, H.; Sheng, F.; Tian, Y.; Zhou, J.; Chen, Y.; Li, S.; Lin, J. Activation of the MAPK11/12/13/14 (P38 MAPK) Pathway Regulates the Transcription of Autophagy Genes in Response to Oxidative Stress Induced by a Novel Copper Complex in HeLa Cells. *Autophagy* **2014**, *10*, 1285–1300, doi:10.4161/auto.28789.
28. Braicu, C.; Buse, M.; Busuioc, C.; Drula, R.; Gulei, D.; Raduly, L.; Rusu, A.; Irimie, A.; Atanasov, A.G.; Slaby, O.; et al. A Comprehensive Review on MAPK: A Promising Therapeutic Target in Cancer. *Cancers (Basel).* **2019**, *11*, doi:ARTN 161810.3390/cancers11101618.
29. Hamdi, M.; Kool, J.; Cornelissen-Steijger, P.; Carlotti, F.; Popeijus, H.E.; van der Burgt, C.; Janssen, J.M.; Yasui, A.; Hoeben, R.C.; Terleth, C.; et al. DNA Damage in Transcribed Genes Induces Apoptosis via the JNK Pathway and the JNK-Phosphatase MKP-1. *Oncogene* **2005**, *24*, 7135–7144, doi:10.1038/sj.onc.1208875.
30. Hammouda, M.B.; Ford, A.E.; Liu, Y.; Zhang, J.Y. The JNK Signaling Pathway in Inflammatory Skin Disorders and Cancer. *Cells* 2020, *9*.
31. Bubici, C.; Papa, S. JNK Signalling in Cancer: In Need of New, Smarter Therapeutic Targets. *Br. J. Pharmacol.* **2014**, *171*, 24–37, doi:10.1111/bph.12432.
32. Saeki, K.; Kobayashi, N.; Inazawa, Y.; Zhang, H.; Nishitoh, H.; Ichijo, H.; Saeki, K.; Isemura, M.; Yuo, A. Oxidation-Triggered c-Jun N-Terminal Kinase (JNK) and P38 Mitogen-Activated Protein (MAP) Kinase Pathways for Apoptosis in Human Leukaemic Cells Stimulated by Epigallocatechin-3-Gallate (EGCG): A Distinct Pathway from Those of Chemically Induced and Recep. *Biochem. J.* **2002**, *368*, 705–720, doi:10.1042/Bj20020101.
33. Sui, X.; Kong, N.; Ye, L.; Han, W.; Zhou, J.; Zhang, Q.; He, C.; Pan, H. P38 and JNK MAPK Pathways Control the Balance of Apoptosis and Autophagy in Response to Chemotherapeutic Agents. *Cancer Lett* **2014**, *344*, 174–179, doi:10.1016/j.canlet.2013.11.019.
34. Varghese, J.; Chattopadhaya, S.; Sarin, A. Inhibition of P38 Kinase Reveals a TNF-Alpha-Mediated, Caspase-Dependent, Apoptotic Death Pathway in a Human Myelomonocyte Cell Line. *J. Immunol.* **2001**, *166*, 6570–6577, doi:DOI 10.4049/jimmunol.166.11.6570.
35. Loría-Bastarrachea, M.I.; Herrera-Kao, W.; Cauich-Rodríguez, J. V; Cervantes-Uc, J.M.; Vázquez-Torres, H.; Ávila-Ortega, A. A TG/FTIR Study on the Thermal Degradation of Poly(Vinyl Pyrrolidone). *J. Therm. Anal. Calorim.* **2011**, *104*, 737–742, doi:10.1007/s10973-010-1061-9.
36. Borodko, Y.; Habas, S.E.; Koebel, M.; Yang, P.; Frei, H.; Somorjai, G.A. Probing the Interaction of Poly (Vinylpyrrolidone) with Platinum Nanocrystals by \mbox{UV}-\mbox{R}aman and \mbox{FTIR}. *J. Phys. Chem. B* **2006**, *110*, 23052–23059.
37. Zhu, X.; Lu, P.; Chen, W.; Dong, J. Studies of UV Crosslinked Poly(N-Vinylpyrrolidone) Hydrogels by FTIR, Raman and Solid-State NMR Spectroscopies. *Polymer (Guildf).* **2010**, *51*, 3054–3063, doi:10.1016/j.polymer.2010.05.006.
38. Han, G.; Chen, Z.-G.; Yang, L.; Wang, L.; Drennan, J.; Zou, J. In-Doped Bi2Se3 Hierarchical Nanostructures as Anode Materials for Li-Ion Batteries. *J. Mater. Chem. A* **2014**, *2*, 7109–7116, doi:10.1039/C4TA00045E.
39. Du, J.; Gu, Z.; Yan, L.; Yong, Y.; Yi, X.; Zhang, X.; Liu, J.; Wu, R.; Ge, C.; Chen, C.; et al. Poly(Vinylpyrollidone)- and Selenocysteine-Modified Bi2 Se3 Nanoparticles Enhance Radiotherapy Efficacy in Tumors and Promote Radioprotection in Normal Tissues. *Adv Mater* **2017**, *29*, doi:10.1002/adma.201701268.
40. Kong, D.; Randel, J.C.; Peng, H.; Cha, J.J.; Meister, S.; Lai, K.; Chen, Y.; Shen, Z.-X.; Manoharan, H.C.; Cui, Y. Topological Insulator Nanowires and Nanoribbons. *Nano Lett.* **2010**, *10*, 329–333, doi:10.1021/nl903663a.
41. Kong, D.; Cha, J.; Lai, K.; Peng, H.; Analytis, J.; Meister, S.; Chen, Y.; Zhang, H.-J.; Fisher, I.; Shen, Z.-X.; et al. Rapid Surface Oxidation as a Source of Surface Degradation Factor for Bi2Se3. *ACS Nano* **2011**, *5*, 4698–4703, doi:10.1021/nn200556h.
42. Zhao, Y.; Pan, H.; Lou, Y.; Qiu, X.; Zhu, J.; Burda, C. Plasmonic Cu2−xS Nanocrystals: Optical and Structural Properties of Copper-Deficient Copper(I) Sulfides. *J. Am. Chem. Soc.* **2009**, *131*, 4253–4261, doi:10.1021/ja805655b.
43. Tian, Q.; Jiang, F.; Zou, R.; Liu, Q.; Chen, Z.; Zhu, M.; Yang, S.; Wang, J.; Wang, J.; Hu, J. Hydrophilic Cu9S5 Nanocrystals: A Photothermal Agent with a 25.7% Heat Conversion Efficiency for Photothermal Ablation of Cancer Cells in Vivo. *ACS Nano* **2011**, *5*, 9761–9771, doi:10.1021/nn203293t.

44. Wells, A.F. *Structural Inorganic Chemistry*; 5th Editio.; Clarendon Press,Oxford, 1990;
45. Roper, D.K.; Ahn, W.; Hoepfner, M. Microscale Heat Transfer Transduced by Surface Plasmon Resonant Gold Nanoparticles. *J. Phys. Chem. C* **2007**, *111*, 3636–3641, doi:10.1021/jp064341w.
46. Liu, Y.; Ai, K.; Liu, J.; Deng, M.; He, Y.; Lu, L. Dopamine-Melanin Colloidal Nanospheres: An Efficient near-Infrared Photothermal Therapeutic Agent for in Vivo Cancer Therapy. *Adv. Mater.* **2013**, *25*, 1353–1359, doi:10.1002/adma.201204683.
47. Yin, W.; Yan, L.; Yu, J.; Tian, G.; Zhou, L.; Zheng, X.; Zhang, X.; Yong, Y.; Li, J.; Gu, Z.; et al. High-Throughput Synthesis of Single-Layer MoS2 Nanosheets as a Near-Infrared Photothermal-Triggered Drug Delivery for Effective Cancer Therapy. *ACS Nano* **2014**, *8*, 6922–6933, doi:10.1021/nn501647j.
48. Zhou, Z.; Yan, Y.; Hu, K.; Zou, Y.; Li, Y.; Ma, R.; Zhang, Q.; Cheng, Y. Autophagy Inhibition Enabled Efficient Photothermal Therapy at a Mild Temperature. *Biomaterials* **2017**, *141*, 116–124, doi:10.1016/j.biomaterials.2017.06.030.
49. Vazquez, C.L.; Colombo, M.I. ASSAYS To ASSESS AUTOPHAGY INDUCTION AND FUSION OF AUTOPHAGIC VACUOLES WITH A DEGRADATIVE COMPARTMENT, USING MONODANSYLCADAVERINE (MDC) AND DQ-BSA. *Methods Enzymol. Autophagy Mamm. Syst. Vol 452, Pt B* **2009**, *452*, 85–95, doi:10.1016/S0076-6879(08)03606-9.
50. Tanida, I.; Ueno, T.; Kominami, E. LC3 and Autophagy. *Methods Mol Biol* **2008**, *445*, 77–88, doi:10.1007/978-1-59745-157-4_4.
51. Gomes-da-Silva, L.C.; Jimenez, A.J.; Sauvat, A.; Xie, W.; Souquere, S.; Divoux, S.; Storch, M.; Sveinbjornsson, B.; Rekdal, O.; Arnaut, L.G.; et al. Recruitment of LC3 to Damaged Golgi Apparatus. *Cell Death Differ.* **2019**, *26*, 1467–1484, doi:10.1038/s41418-018-0221-5.
52. Yang, J.; Nie, J.; Ma, X.L.; Wei, Y.Q.; Peng, Y.; Wei, X.W. Targeting PI3K in Cancer: Mechanisms and Advances in Clinical Trials. *Mol. Cancer* **2019**, *18*, doi:ARTN 2610.1186/s12943-019-0954-x.